

 Open access • Journal Article • DOI:10.1007/S10971-015-3737-X

## Sol-gel synthesis and characterization of the delafossite CuAlO<sub>2</sub> — Source link

N. Benreguia, Antoine Barnabé, Mohamed Trari

**Institutions:** University of Toulouse

**Published on:** 06 Jun 2015 - Journal of Sol-Gel Science and Technology (Springer US)

**Topics:** Delafossite, Nanocrystalline material, Constant phase element, Dielectric spectroscopy and Crystallite

Related papers:

- [P-type electrical conduction in transparent thin films of CuAlO<sub>2</sub>](#)
- [Electrochemical intercalation of O<sub>2</sub><sup>-</sup> in CuAlO<sub>2</sub> single crystal and photoelectrochemical properties](#)
- [Optical and electrical properties of mechanochemically synthesized nanocrystalline delafossite CuAlO<sub>2</sub>.](#)
- [The photoconductivity properties of transparent Ni doped CuAlO<sub>2</sub> films](#)
- [p-Type Optoelectronic and Transparent Conducting Oxide Properties of Delafossite CuAl<sub>1/2</sub>Fe<sub>1/2</sub>O<sub>2</sub>](#)

Share this paper:    

View more about this paper here: <https://typeset.io/papers/sol-gel-synthesis-and-characterization-of-the-delafossite-1ce1f1ny36>




## Open Archive Toulouse Archive Ouverte (OATAO)

OATAO is an open access repository that collects the work of Toulouse researchers and makes it freely available over the web where possible

This is an author's version published in: <http://oatao.univ-toulouse.fr/23649>

**Official URL:** <https://doi.org/10.1007/s10971-015-3737-x>

**To cite this version:**

Benreguia, Nadia and Barnabé, Antoine  and Trari, Mohamed *Sol-gel synthesis and characterization of the delafossite CuAlO<sub>2</sub>*. (2015) *Journal of Sol-Gel Science and Technology*, 75 (3). 670-679. ISSN 0928-0707

Any correspondence concerning this service should be sent to the repository administrator: [tech-oatao@listes-diff.inp-toulouse.fr](mailto:tech-oatao@listes-diff.inp-toulouse.fr)

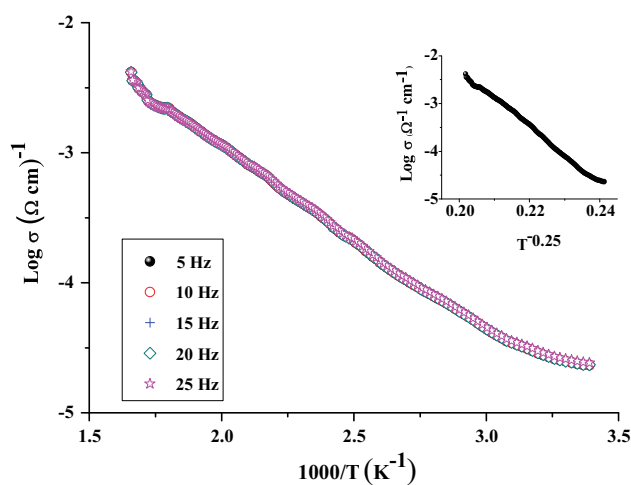
# Sol–gel synthesis and characterization of the delafossite $\text{CuAlO}_2$

N. Benreguia<sup>1</sup> · A. Barnabé<sup>2</sup> · M. Trari<sup>1</sup>

**Abstract** Nanocrystalline  $\text{CuAlO}_2$  is synthesized by sol–gel method using ethylene glycol as solvent. The stages of formation are followed by thermal analysis. The X-ray diffraction pattern of the powder heat-treated at 1100 °C shows a single phase, indexed in a rhombohedral symmetry ( $R\bar{3}m$ ). The apparent crystallite size ( $57 \pm 8$  nm) is determined from the Williamson–Hall plot. The direct optical transition ( $\approx 3.69$  eV), evaluated from the diffuse reflectance spectrum, is attributed to the charge transfer ( $\text{O}^{2-}: 2p \rightarrow \text{Cu}^+: 4s$ ). The oxide is *p*-type semiconductor, and the conduction occurs predominantly by small polaron hopping between mixed valences  $\text{Cu}^{2+/+}$ , due to oxygen insertion in the layered crystal. The photoelectrochemical characterization gives a flat band of 0.20  $\text{V}_{\text{SCE}}$  and a hole density of  $1.13 \times 10^{18} \text{ cm}^{-3}$ . The semicircle centered on the real axis, in the electrochemical impedance spectroscopy (EIS), is due to the absence of constant phase element with a pure capacitive behavior. The straight line at 35° at low frequencies is attributed to the diffusion in the layered structure.

**Graphical Abstract** Temperature dependence of the electrical conductivity for  $\text{CuAlO}_2$  synthesized by sol–gel method. Inset: the variable range hopping at low temperatures. The sol–gel method has been successfully employed

for the preparation of  $\text{CuAlO}_2$ . The thermal variation of the conductivity indicates a semiconducting behavior which is frequency independent. At low temperature, a variable range hopping involves electrons jump over large distances according to the Mott law  $\sigma = \sigma_0 \exp\left(\frac{T_0}{T}\right)^{0.25}$ .



**Keywords** Nanocrystalline · Delafossite  $\text{CuAlO}_2$  · Sol–gel method · Semiconductor · Photoelectrochemical · Nyquist–Bode plots

✉ M. Trari  
solarchemistry@gmail.com

<sup>1</sup> Laboratory of Storage and Valorization of Renewable Energies, Faculty of Chemistry (USTHB), BP 32, 16111 Algiers, Algeria

<sup>2</sup> Centre Inter-universitaire de Recherche et d'Ingénierie des Matériaux (CIRIMAT)-UMR CNRS 5085, Université de Toulouse III Paul Sabatier, 118 Route de Narbonne, 31062 Toulouse Cedex 09, France

## 1 Introduction

Extensive research is being carried out to improve the photocatalytic properties of oxides, and special interest has been focused on the layered structures [1]. In this respect, the delafossite  $\text{CuMO}_2$ , where M denotes a

trivalent metal, is thermodynamically stable phases crystallizing in a two-dimensional lattice and has received growing attention over the last decade [2–4]. They occupy an important place in various fields by virtue of the diversity of physical properties and have a great promise in the solar energy conversion [5–7] and environmental protection [8, 9]. However, the lifetime of the photocarriers is short because they move in a narrow Cu-3*d* band ( $\sim 2$  eV width) with a small diffusion length and a low hole mobility ( $\sim 10^{-5}$  cm<sup>2</sup> V<sup>-1</sup> s<sup>-1</sup>) [10]; this inhibits considerably the light-to-energy conversion and leads to low efficiencies. So, the strategy is to synthesize the oxide by chemical route in order to shorten the path the photocarriers have to diffuse to reach the interface. In this respect, a considerable improvement has been made in the synthesis of photoactive materials with small crystallite sizes and large specific surface areas [11–13]. With the advent of nanotechnology, the sol–gel method has gained recognition in the solid-state chemistry and a review of advantages has been given recently by Koseva [14]. The method has broadened the field of photovoltaic and photocatalysis by controlling the crystallite size, and this is particularly advantageous for small polaron oxides such as the delafossites and spinels [15, 16]. The mechanism involves the hydrolysis of molecular precursors followed by a polycondensation to glass-like form. The advantage is that the reagents are mixed at an atomic level, and this should increase the reaction rate and favor the formation of nanocrystallites. In addition, the calcination temperature strongly influences the physical properties of the material. In this work, we have undertaken a detailed study of the structural, optical and photoelectrochemical (PEC) properties of CuAlO<sub>2</sub> prepared by sol–gel method.

## 2 Experimental

All reagents were obtained from commercial sources and used without any further treatment. CuAlO<sub>2</sub> was prepared with a slightly modified sol–gel method employed previously by some of us [17]. CuO (Fluka, >98 %), preheated at 400 °C, was dissolved in a minimum of concentrated HNO<sub>3</sub> (6 N, BDH) and mixed to Al(NO<sub>3</sub>)<sub>3</sub>·9H<sub>2</sub>O (Merck, 99 %) in a molar ratio (Cu/Al = 0.025/0.025). Then, the mixture was dissolved at room temperature in 60 mL of ethylene glycol (BDH) and heated under moderate stirring (350 rpm) at 70 °C under reflux for 6 h, and the viscous solution was dried at 120 °C for 7 days. The gelation occurred on a magnetic-stirring hot plate till a brown color appeared. The amorphous powder was heated at 450 °C to eliminate the nitrates and organic matter. Then, the powder was fired at 1100 °C (16 h) with intermediate regrinding in

a muffle furnace (Nabertherm); the end product exhibits a gray color.

## 3 Characterizations

### 3.1 X-ray diffraction

The X-ray diffraction (XRD) data were collected with a Bruker D4 Endeavor Advance diffractometer over the angular range  $2\theta$  (15°–100°) using CuK <sub>$\alpha$</sub>  radiation ( $\lambda = 0.154178$  nm) with a step size of 0.02° and a counting time of 2s/step. The patterns were compared with the JCPDS Cards to check the completion of the reaction using a Bruker Eva program. The structural refinements were made with the Rietveld analysis implemented in the Full-Prof–WinPLOTR program.

### 3.2 Thermogravimetric analysis

Thermogravimetric analysis of the amorphous powder, heated at 450 °C, was carried out on a Setaram TAG 1750 instrument in an alumina crucible up to 1000 °C (heating rate of 5 °C min<sup>-1</sup>).

### 3.3 Scanning electron microscopy (SEM)

The microstructure was visualized by scanning electron microscopy (SEM, JEOL 6510 LV microscope) operating at an acceleration voltage of 20 kV. The crystallites size was evaluated from the Williamson–Hall plot which takes into account all XRD peaks and eliminates the collapsed ones. The specific surface area is based on the formation of gas monolayer on the oxide surface. The corresponding volume was measured by adsorption/desorption of nitrogen (30 % N<sub>2</sub> in He) at 77 K with a Micromeritics Flowsorb 2300 equipment.

### 3.4 FTIR spectroscopy

The FTIR spectrum of the powder was recorded with a Nicolet spectrometer 6700. The powder was pressed into disk using dried spectroscopic KBr and scanned in the absorbance mode over the range (400–4000 cm<sup>-1</sup>).

### 3.5 Raman spectroscopy

The Raman spectrum was recorded with a Jobin–Yvon T64000 spectrophotometer at room temperature in the range (200–1000 cm<sup>-1</sup>) with 514.5 nm line Ar<sup>+</sup> laser excitation from a Spectra Physics Krypton ion laser. The compound was studied with a low laser power (4 W); the beam was focused onto the sample using the macroscopic

configuration of the apparatus; and no damage of the material by the laser was observed.

### 3.6 Optical properties

The diffuse reflectance spectrum was recorded with a double-beam UV–Vis spectrophotometer (SPECORD 200 Plus) attached to an integrating sphere, and PTFE was used as reference. The data were collected in the range (300–1200 nm).

### 3.7 Electrical properties

The electrical conductivity ( $\sigma$ ) was measured by the two-probe method under argon atmosphere using an Agilent LCR meter 4363B equipment.  $\text{CuAlO}_2$  was used in the form of pellets ( $\varnothing = 13\text{-mm}$ -diameter disk and  $\sim 1\text{ mm}$  thickness), sintered at  $1100\text{ }^\circ\text{C}$ . The pellet dimensions, measured with a Vernier and weighed in an analytical balance ( $10^{-4}\text{ g}$ ), were used to estimate the bulk density. A compactness of 80 % or more was obtained.

### 3.8 Photoelectrochemical properties

The pellet showed good mechanical properties, and the back contact with copper wires was made with silver paint. The working electrode ( $\text{CuAlO}_2$ ,  $1.32\text{ cm}^2$ ) was encapsulated in a glass tube and isolated by epoxy resin. A three-electrode cell, including Pt electrode (Tacussel,  $1\text{ cm}^2$ ) and a saturated calomel electrode, was used for plotting the intensity potential  $J(V)$  curves. The working electrode was illuminated by a halogen tungsten lamp (200 W) through a flat window, and the potential was monitored by a Voltalab PGZ 301 potentiostat (Radiometer analytical). The KOH solution (0.5 M) was flushed continuously with nitrogen, and the experiments were performed at room temperature. The Mott–Schottky characteristic was plotted at a frequency of 10 kHz. Sinusoidal perturbations of  $\pm 0.01\text{ V}$  were applied between  $10^{-3}$  and  $10^5\text{ Hz}$ ; the Nyquist data were analyzed by the ZView software.

## 4 Results and discussion

### 4.1 Microstructure and crystal structure

The sol–gel method gives a better crystallinity, precludes the phase aggregation and leads to submicron dimension with a narrow size distribution. Through a careful selection of synthesis conditions, it has been found that  $\text{CuAlO}_2$  can be prepared as a homogeneous single phase. The heat treatment of the amorphous powder at  $450\text{ }^\circ\text{C}$  in air permits to remove water and decomposes the nitrates.

According to the XRD pattern (Fig. 1a, Inset), there are only the reflections of  $\text{CuO}$  (tenorite) and amorphous  $\text{Al}_2\text{O}_3$ ; no other aluminum-based phases such as hydroxide, oxide–hydroxide or oxide have been detected. So, one can conclude that the diffusivity of oxygen into the precursor powder is low at  $450\text{ }^\circ\text{C}$  and a heat treatment at higher temperature is required to form mixed copper–aluminum oxide such as the spinel  $\text{CuAl}_2\text{O}_4$ . The TGA plot of the powder treated at  $450\text{ }^\circ\text{C}$  in air shows a progressive weight loss from room temperature up to  $600\text{ }^\circ\text{C}$ , compatible with the dehydration of the boehmite [18]. However, the weight loss at  $\sim 740\text{ }^\circ\text{C}$  remains unexplained.

The XRD pattern (Fig. 1b) of the powder treated at  $1000\text{ }^\circ\text{C}$  shows the coexistence of  $\text{CuAl}_2\text{O}_4$  and  $\text{CuO}$ . Therefore, in air,  $\text{Cu}^{2+}$ -based oxides are the most stable phases in agreement with the diagram temperature versus  $\log p\text{O}_2$  previously reported for the Cu–Al–O system [19–21]. Chen et al. [22] also reported that the XRD analysis of amorphous powder for the preparation of Cu–Al–O

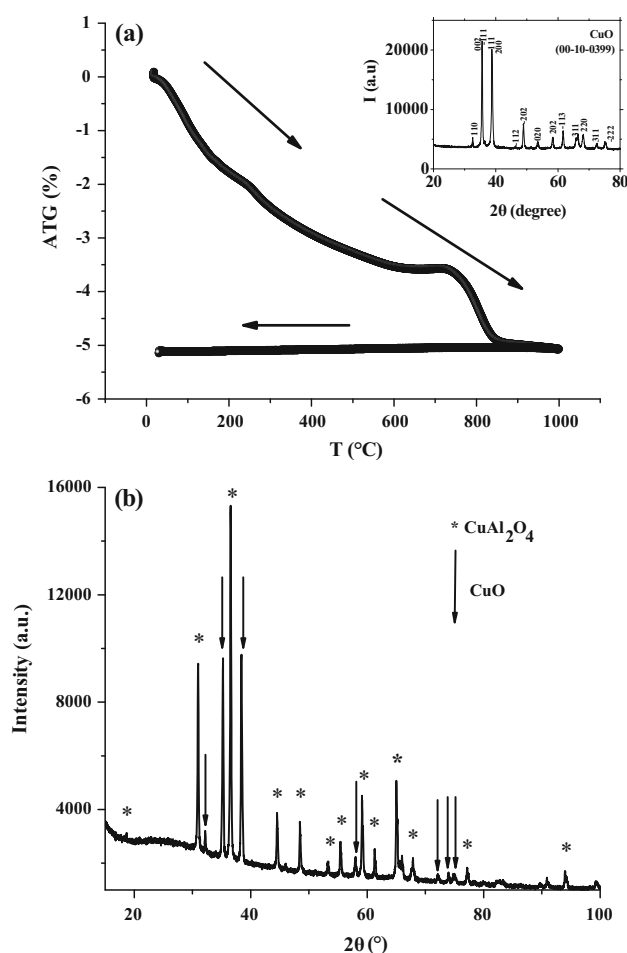
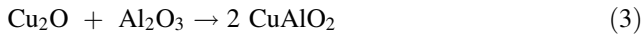


**Fig. 1** a TGA plots indicating the evolution of the mixture. *Inset* the XRD pattern of the amorphous powder treated at  $450\text{ }^\circ\text{C}$  in air. **b** The XRD pattern at  $1000\text{ }^\circ\text{C}$  indicating a mixture of  $\text{CuAl}_2\text{O}_4$  and  $\text{CuO}$

thin films revealed the presence of CuO (tenorite) and  $\text{CuAl}_2\text{O}_4$  at 700 °C under different atmospheres ( $\text{N}_2$ ,  $\text{O}_2$ , air), while the delafossite  $\text{CuAlO}_2$  appears at 800 °C only under  $\text{N}_2$  flow. In air,  $\text{CuAlO}_2$  could be stabilized between 1000 and 1250 °C, and its formation can be summarized as follows [19]:



The powder calcined at 1100 °C (16 h) exhibits a gray color, characteristic of pure delafossite  $\text{CuAlO}_2$  in

agreement with the JCPDS Card N° 075-2356 (Fig. 2a). The refined lattice constants in the rhombohedral description (SG:  $R\bar{3}m$ ):  $a = 0.2852 \text{ nm}$  and  $c = 1.6830 \text{ nm}$  are in good agreement with those given in the literature [23].  $\text{CuAlO}_2$  crystallizes in a hexagonally close-packed lattice with 3R polytype;  $\text{Al}^{3+}$  is located at centers of trigonally distorted octahedra linked by edge-sharing, forming infinite  $\infty[\text{AlO}_2]$  sheets in the (001) planes (Fig. 3).  $\text{Cu}^+$  connects linearly two adjacent layers, leading to  $(\text{CuO}_2)^{3-}$  dumbbells parallel to the  $c$ -axis and giving  $\text{CuAlO}_2$  anisotropic properties. Selected interatomic distances and bond angles are reported in Table 1. The Cu–O length (0.1860 nm) agrees perfectly with that calculated from the ionic radii of  $^{\text{II}}\text{Cu}^+$  (0.046 nm) and  $^{\text{IV}}\text{O}^{2-}$  (0.1380 nm) [24]. Such agreement confirms the ionicity of the chemical bond and the small polarizability of ions and the electron localization. The  $\text{AlO}_6$  octahedron is flattened, and the deformation of the symmetry  $D_{3d}$  is correlated with the strength of the Al–O bond:  $\frac{d_{\text{O}-\text{oi}}}{d_{\text{O}-\text{oiv}}} = 1.126$  [25], where  $d_{\text{O}-\text{oi}}$  is the edge of  $\text{AlO}_6$  octahedron in the (a, b) plane and  $d_{\text{O}-\text{oiv}}$  the length connecting two oxygen atoms belonging to two consecutive layers containing  $\text{Al}^{3+}$  ions (Fig. 3, Inset). The covalency of the Al–O leads to a decrease in the formal charge, resulting in a weaker repulsion between  $\text{Al}^{3+}$  ions and a diminution of the O–Al–O angle ( $\sim 83^\circ$ ) instead of  $90^\circ$ . The crystallite size of  $\text{CuAlO}_2$  ( $57 \pm 8 \text{ nm}$ ), evaluated from the Williamson–Hall plot by extrapolation to  $\theta = 0$ , indicates nanocrystallites (Fig. 2b). Assuming spherical and non-porous crystallites as shown in the SEM image (Fig. 4), the specific surface area ( $S = \frac{6}{\rho_{\text{exp}} \times D}$ ) averages  $21 \text{ m}^2 \text{ g}^{-1}$ . Such result gives the surface of the crystallites. However, the specific surface area, determined by the BET method, is much smaller ( $S_{\text{BET}} = 1.39 \text{ m}^2 \text{ g}^{-1}$ ) because it is relative to the surface of the grains which are agglomerates of crystallites. Indeed, the SEM image clearly shows two types of granular grains with 0.5–1  $\mu\text{m}$  dimensions; large  $\text{CuAlO}_2$  crystals with well-defined natural crystalline faces are formed which corroborate the strong agglomeration, a not surprising given the high temperature to synthesize  $\text{CuAlO}_2$ .

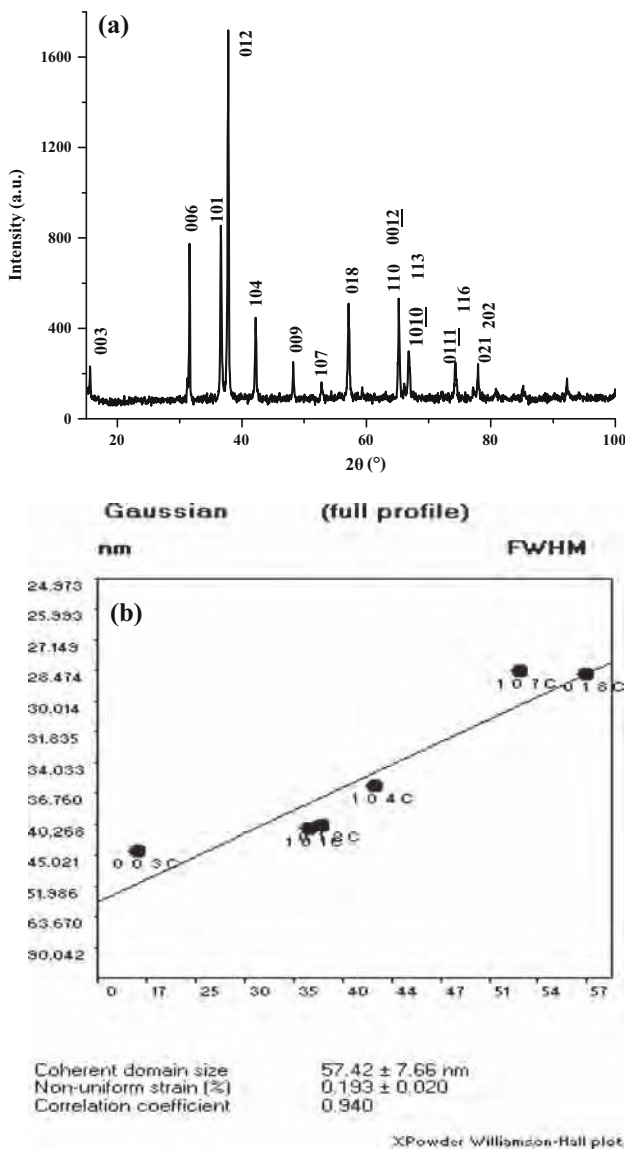


**Fig. 2** a The XRD pattern of the single-phase  $\text{CuAlO}_2$  synthesized by sol-gel method at 1100 °C for 16 h. b The crystallite size determined from the Williamson–Hall plot

## 4.2 FTIR measurement

The FTIR spectrum gives valuable information on the metal–oxygen stretching as well as the sites of ions. The Cu–O stretching peak at  $554 \text{ cm}^{-1}$  is characteristic of  $\text{Cu}^+$  in linear coordination [26]. The absorption peaks at 772 and  $949 \text{ cm}^{-1}$  (Fig. 5) arise from Al–O stretching vibration in distorted  $\text{AlO}_6$  octahedra close to those reported elsewhere [27, 28]. The broad band at  $3460 \text{ cm}^{-1}$  is due to O–H stretching vibration, while the bending vibration of physisorbed water is observed at  $1637 \text{ cm}^{-1}$  [29].



**Fig. 3** Structure of the delafossite  $\text{CuAlO}_2$ . The blue polyhedra represents edge-shared  $\text{Al}^{3+}\text{O}_6$  distorted octahedra linearly coordinated by  $\text{Cu}^+$  cations. *Inset* the flattened  $\text{AlO}_6$  octahedra

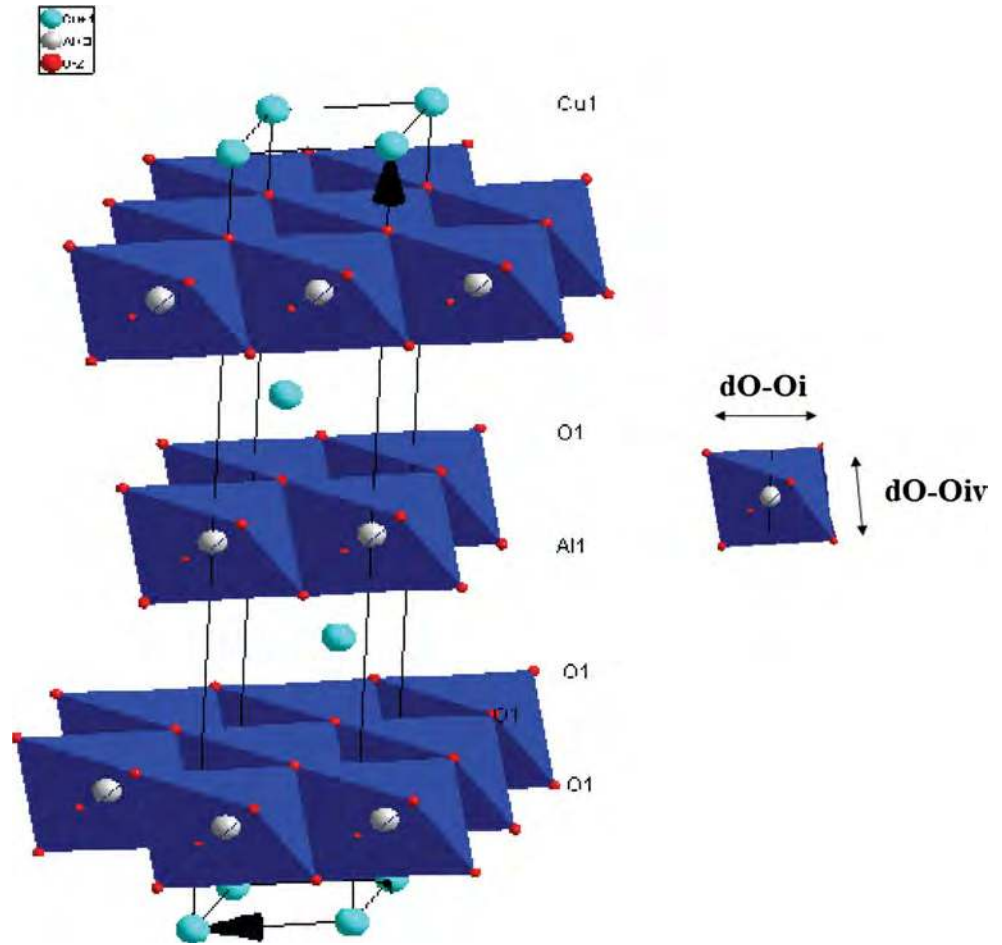


**Table 1** Bond distances and angles in the delafossite  $\text{CuAlO}_2$

Cu–O	(×2)	1.861(1)
$\text{Al}^{\text{II}}\text{–O}$	(×6)	1.912(1)
Cu–Cu <sup>I</sup>	(×6)	2.860(1)
O–O <sup>I</sup>	(×6)	2.860(1)
O–O <sup>IV</sup>	(×6)	2.539(2)
O– $\text{Al}^{\text{II}}\text{–O}^{\text{I}}$	(×6)	96.81°
O– $\text{Al}^{\text{II}}\text{–O}^{\text{IV}}$	(×6)	83.19°
Cu–O– $\text{Al}^{\text{II}}$	(×3)	120.28°
$\text{Al}^{\text{II}}\text{–O–Al}^{\text{II}}$	(×3)	96.81°

### 4.3 Raman spectroscopy

The delafossites with four atoms per unit formula present 12 normal modes. The group theory decomposes a general mode at the Brillouin zone center ( $\Gamma = A_{1g} + E_g + 3A_{2u} + 3A_u$ ). The modes A induce movement in the direction of Cu–O bond along the c-axis, whereas the double degenerate E modes describe vibrations in the perpendicular direction [30]. The existence of an inversion

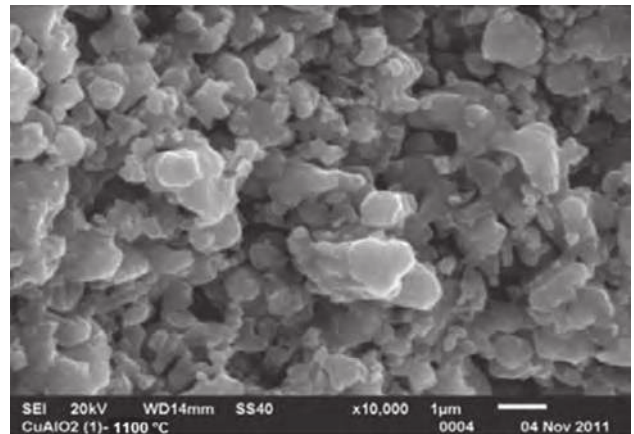


**Fig. 4** SEM image of  $\text{CuAlO}_2$  powder synthesized by sol-gel method at 1100 °C

center in the structure classifies normal modes as a function of their parity. Odd modes, denoted with the subscript  $u$ , are infrared active and include acoustic modes ( $A_{2u} + A_u$ ).

The Raman spectrum of  $\text{CuAlO}_2$  is shown in Fig. 6. Three bands are identified as  $\sigma(A_{1g})$  at  $773\text{ cm}^{-1}$ ,  $\sigma(E_g)$  at

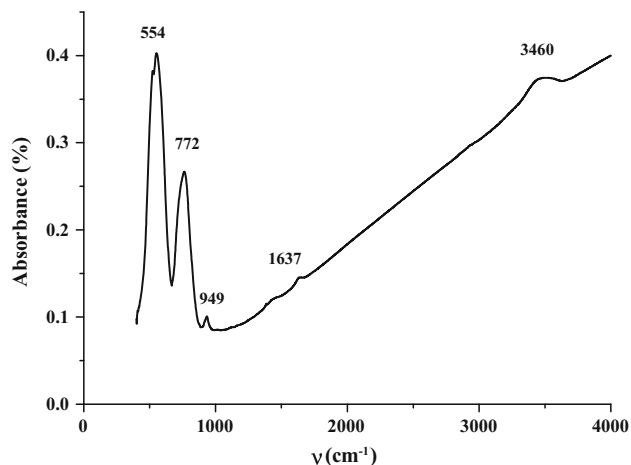


**Fig. 5** Infrared spectrum of CuAlO<sub>2</sub> synthesized by sol-gel method at 1100 °C

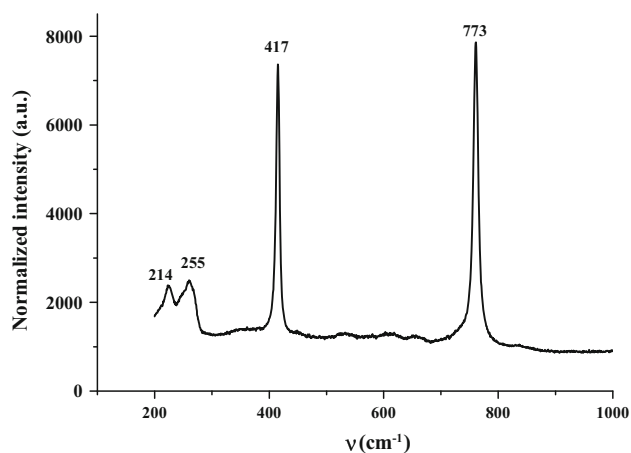


**Fig. 6** Raman spectrum of CuAlO<sub>2</sub> at room temperature

417 cm<sup>-1</sup> [31] and  $\sigma(A_g)$  at 214 cm<sup>-1</sup> [32]. They may be associated with the edge-sharing Al<sup>III</sup>O<sub>6</sub> octahedra and O–Cu<sup>I</sup>–O linear bond. We have also found a further peak at 255 cm<sup>-1</sup> assigned to Al<sub>2</sub>O<sub>3</sub>, very close to that reported by Nagabhushana et al. (253 cm<sup>-1</sup>) [33]. It may be due to the fact the vibrational spectrum is modified by a slight change in the crystal structure [34]. In order to attribute the vibration mode, we have made a comparison with isostructural compounds, namely  $\alpha$ -Al<sub>2</sub>O<sub>3</sub> and  $\alpha$ -Fe<sub>2</sub>O<sub>3</sub>. The peak observed at 255 cm<sup>-1</sup> could be assigned to the  $E_g$  mode of  $\alpha$ -Al<sub>2</sub>O<sub>3</sub> and is very close to that reported for  $\alpha$ -Fe<sub>2</sub>O<sub>3</sub> by Lübke et al. [35].

#### 4.4 Optical properties

The optical gap of CuAlO<sub>2</sub> is determined from the diffuse reflectance ( $R$ ) using the Kubelka–Munk equation:

$$F(R) = \frac{(1 - R)^2}{2R} \quad (4)$$

The relation between the optical absorption coefficient ( $\alpha$ ), the gap ( $E_g$ ) and the incident energy ( $h\nu$ ) is given by [36]:

$$(\alpha h\nu)^m = A \times (h\nu - E_g) \quad (5)$$

where  $A$  is a constant and  $m$  depends on the type of transition:  $m = 1/2$  for indirect transition and  $m = 2$  for direct transition. A direct transition (3.69 eV) occurs between the deep lying O<sup>2-</sup>: 2p orbital and Cu<sup>+</sup>: 4s orbital, attributed to the charge transfer (Fig. 7), in agreement with previous results [37–40].

#### 4.5 Electrical properties

The distance between the Cu<sup>+</sup> ions ( $=a$ -parameter) is more than the length required for the onset of metallic state and CuAlO<sub>2</sub> is expected to be insulator. However, the composition slightly deviates from the stoichiometry by oxygen intercalation due to the layered structure, leading to enhanced electrical conductivity [41]. Such migration needs diffusion path within the parent network in the basal plans along the [010] direction, and Cu<sup>2+</sup> is formed to maintain the electro-neutrality. However, we are unable to quote the over stoichiometry by chemical analysis [42]<sup>1</sup>.

The conductivity increases with increasing temperature, characterizing a semiconducting behavior which is frequency independent (Fig. 8). The Arrhenius law is obeyed over the range (300–500 K) with activation energy ( $E_a$ ) of 0.26 eV, close to that reported previously [27, 43, 44]. Therefore, the enhanced conductivity arises from the thermally activated hole density ( $N_A$ ) rather than the mobility ( $\mu_h$ ). Owing to the electron–phonon interaction, the carriers move by phonon assisted hopping polaron between nearest neighbors [45]. A small polaron is generated when the electron is trapped locally by a lattice distortion which moves as a whole entity. At low temperature, a variable range hopping is predicted which involves hopping over large distances than between nearest neighbors (Fig. 8, Inset); the partial localization is due to cation disorder according to the Mott law:

$$\sigma = \sigma_0 \exp\left(\frac{T_0}{T}\right)^\gamma, \quad \gamma = 0.25 \quad (6)$$

#### 4.6 Photoelectrochemical properties

Because of its great potential in the PEC conversion, it is of interest to characterize CuAlO<sub>2</sub> photoelectrochemically.

<sup>1</sup> CuAlO<sub>2</sub> is stable over the whole pH range (–1, +14). Even in concentrated HClO<sub>4</sub>, the amount of Cu<sup>2+</sup> is too small for a reliable determination by atomic absorption.



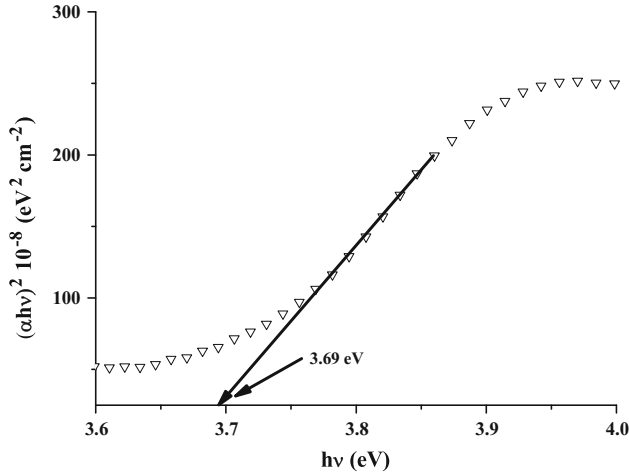


**Fig. 7** Determination of the direct optical transition of CuAlO<sub>2</sub> prepared by sol-gel method

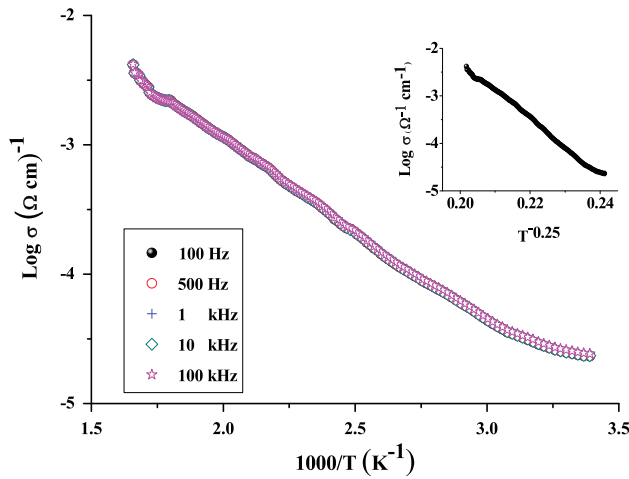
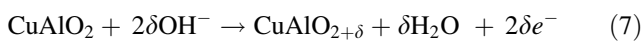


**Fig. 8** Temperature dependence of the electrical conductivity for CuAlO<sub>2</sub> synthesized by sol-gel method. *Inset* the variable range hopping at low temperatures

The current voltage  $J(V)$  characteristic is plotted in KOH (0.5 M) solution in an effort to determine the electrochemical processes at the interface. The dark current ( $<1 \text{ mA cm}^{-2}$ ) is due to thermal excitation across the energy  $E_g$ , and the blocking contact with the electrolyte is consistent with a good electrochemical stability. The electrochemical behavior of CuAlO<sub>2</sub> shows two irreversible anodic peaks (Fig. 9). The first peak at  $\sim 0.62 \text{ V}$  is due to an internal redox process, i.e., oxygen intercalation in the layered lattice with concomitant oxidation of Cu<sup>+</sup> according to the reaction:



where  $\delta$  stands for the amount of intercalated oxygen. The quantity of electricity under the peak is evaluated to

$0.59 \text{ mC cm}^{-2}$  and corresponds to the oxidation of  $3.69 \times 10^{15} \text{ at. Cu}^+ \text{ cm}^{-2}$ . The peak at  $\sim 0.85 \text{ V}$ , on the reverse scan, is due to the reduction of Cu<sup>2+</sup> followed subsequently by oxygen deintercalation. This observation shows that the electron transfer corresponds to a sluggish system because of the large difference between peaks ( $\sim 0.35 \text{ V}$ ) compared with the reversible value ( $0.059 \text{ V/n}$ ) although the ratio of anodic to cathodic current heights is close to unity,  $n$  being the number of exchanged electrons. Below  $-1 \text{ V}$ , the current shoots up considerably; due to H<sub>2</sub> evolution, gas bubbles were noticeable on the electrode. The small exchange current  $J_0$  ( $0.2 \mu\text{A cm}^{-2}$ ) and the high polarization resistance ( $=10.7 \text{ k}\Omega \text{ cm}^2$ ) indicate a long-lived material (Fig. 9, Inset). The current  $J_0$  is equivalent to the rate constant of the electron transfer at zero potential.

The increase in the photocurrent ( $J_{\text{ph}}$ ) along the cathodic polarization is in conformity with  $p$ -type conduction which takes its origin from the oxygen insertion (Fig. 9) [46]. The flat-band potential ( $V_{\text{fb}} = 0.20 \text{ V}$ ) and the hole density ( $N_A = 1.13 \times 10^{18} \text{ cm}^{-3}$ ) are provided, respectively, from the intercept of the potential axis at  $C^{-2} = 0$  and the slope of the Mott-Schottky characteristic (Fig. 10):

$$C^{-2} = \left( \frac{2}{e\epsilon\epsilon_0 N_A} \right) \left( V - V_{\text{fb}} - \frac{kT}{e} \right) \quad (8)$$

where  $k$  is the Boltzmann constant,  $T$  the absolute temperature,  $\epsilon_0$  the permittivity of free space and  $e$  the charge of an electron. The permittivity of CuAlO<sub>2</sub> ( $\epsilon \sim 35$ ) was determined from the dielectric measurements. The negative slope gives additional support to  $p$ -type conductivity. The  $N_A$  value should give a thermoelectrical power ( $S$ ) of  $\sim 800 \mu\text{V K}^{-1}$ , compatible with previous works [47, 48]:

$$S = \left( \frac{k}{e} \right) \ln \frac{N_0}{N_A} \quad (9)$$

The hole mobility  $\mu_h = \left( \frac{\sigma_{300\text{K}}}{e \times N_0} \right)$  of  $1.35 \times 10^{-4} \text{ cm}^2 \text{ V}^{-1} \text{ s}^{-1}$  is typical of delafossite oxides [48]; the concentration of available sites ( $N_0$ ) is equal to the number of linear Cu<sup>+</sup> units. The low mobility  $\mu_h$ , defined as the mean drift velocity in an electric field of unit force, is a hallmark of a conduction mechanism by small polaron hopping.

The EIS measurement is done at the open-circuit potential in KOH medium and permits to determine the contributions of the electrolyte, bulk and grain boundaries. The semicircle at high frequencies is attributed to the faradic charge transfer at the junction CuAlO<sub>2</sub>/solution. The center of the circle is localized on the real axis, indicating the absence of constant phase element, i.e., a pure capacitive behavior where the electron hopping occurs by crossing a high potential barrier. However, the straight line at low frequencies is due to a resistive and slow diffusion of electroactive species in the layered structure since the angle ( $35^\circ$ ) is below that for Warburg impedance ( $45^\circ$ ).

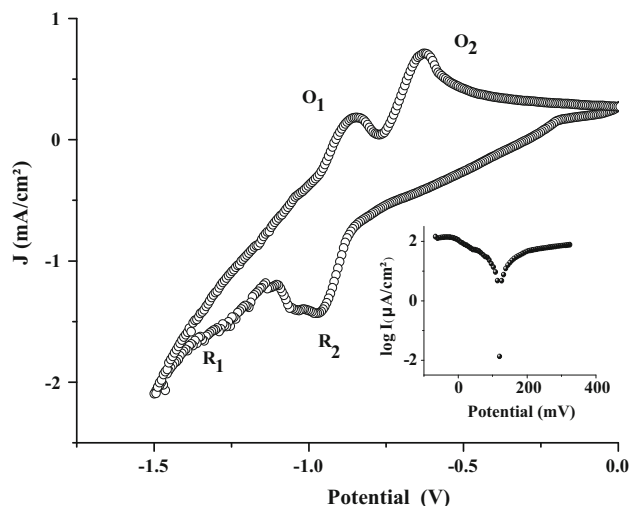


**Fig. 9** Cyclic J (V) characteristic of  $\text{CuAlO}_2$  in KOH solution (0.5 M) plotted under  $\text{N}_2$  bubbling at 25 °C, scan rate 10 mV/s. Inset the semilogarithmic plot ( $\log J$ -V)

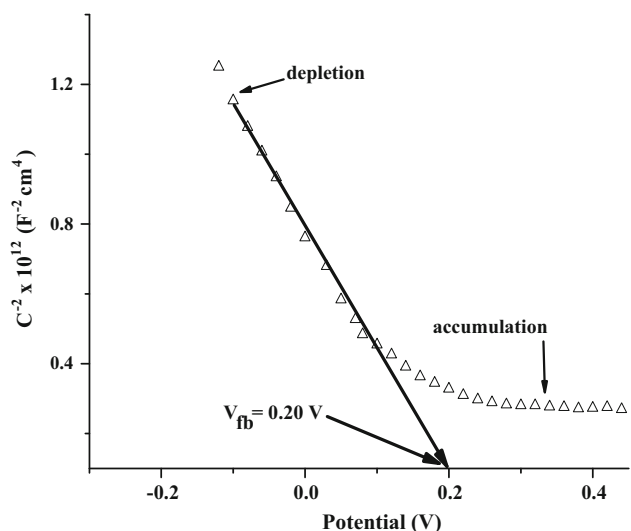


**Fig. 10** Mott-Schottky plot of  $\text{CuAlO}_2$  in KOH (0.5 M) solution at 10 kHz. The depletion and accumulation zones are shown

The equivalent electrical circuit is reported in Fig. 11a (Inset);  $R_{ct}$  is the resistance of the charge transfer ( $12.3 \text{ k}\Omega \text{ cm}^2$ ) and  $R_{el}$  the electrolyte solution ( $0.46 \text{ k}\Omega \text{ cm}^2$ ); the latter is due to the high mobility of  $\text{OH}^-$  ions ( $199 \text{ }\Omega^{-1} \text{ cm}^2 \text{ mol}^{-1}$ ).

The process is also represented in the Bode plan ( $\log Z$  vs.  $\log$  frequency). The phase angle approaching  $-23^\circ$  (Fig. 11b) is characteristic of a compact and non-porous semiconductor with a small rugosity, in agreement with the high compactness. The decrease in  $Z$  with increasing the frequency indicates an enhanced electrical conductivity and a lowering of the potential barrier.

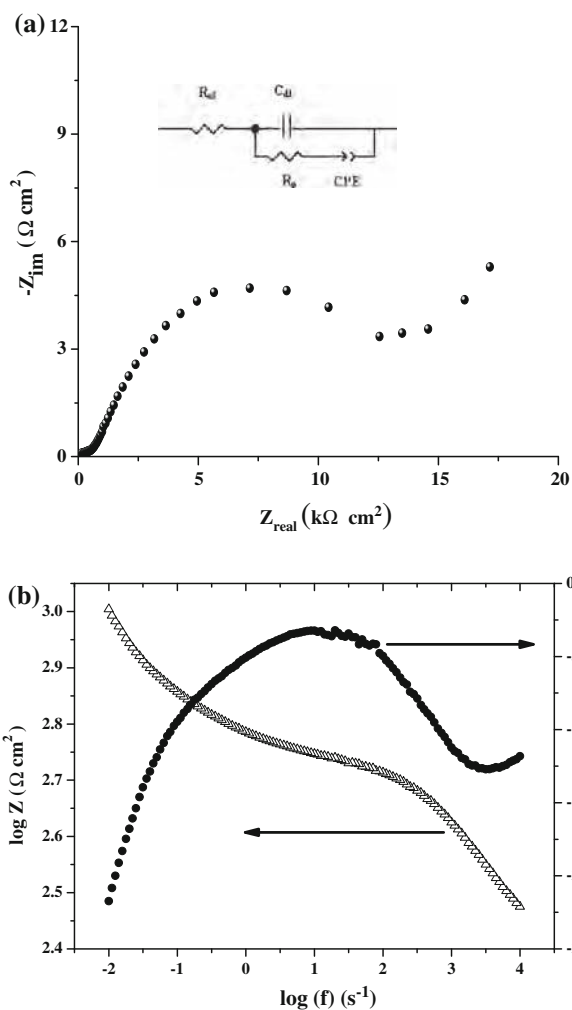


**Fig. 11** a The Nyquist plot of  $\text{CuAlO}_2$  in KOH (0.5 M) solution. Inset the equivalent electrical circuit. b The Bode plot

The cathodic potential of the conduction band ( $V_{fb} - e \times E_g$ ) of  $\text{CuAlO}_2$  predicts a high photocatalytic performance. Such results indicate a great potentiality of  $\text{CuAlO}_2$  in photocatalysis. Indeed, the oxide has been tested successfully for the removal of heavy metal under visible light and the results will be reported consecutively.

## 5 Conclusions

The synthesis of nanocrystallites  $\text{CuAlO}_2$  by sol-gel method is reported, and both the physical and photoelectrochemical characterizations are investigated. The oxide crystallizes in the delafossite structure with nanomorphology and submicron-sized crystallites. The direct optical gap is determined from the diffuse reflectance. The electrical conduction occurs by small polaron hopping between mixed copper valences due to the oxygen intercalation in

the two-dimensional structure. The increase in the photocurrent along the cathodic polarization indicates p-type conductivity which takes its origin from oxygen insertion in the layered lattice. The electrochemical impedance spectroscopy shows the predominance of the charge transfer.  $\text{CuAlO}_2$  has environmental advantages and a gap appropriately matched to the sun spectrum which makes the oxide promising for the solar energy conversion.

**Acknowledgments** The authors thank the Ministry of Scientific Research (Algeria) for the research grant and the OVM group (Mixed Valence Oxide) at CIRIMAT-UMR CNRS at Paul Sabatier University Toulouse III (France) for welcoming one of the authors (N. B.), for their collaboration.

## References

- Rajeshwar K (2007) Hydrogen generation at irradiated oxide semiconductor solution interfaces. *J Appl Electrochem* 37: 765–787
- Shahriari DY, Barnabé A, Mason TO, Poepelmeier KR (2001) A high-yield hydrothermal preparation of  $\text{CuAlO}_2$ . *Inorg Chem* 40:5734–5735
- Bellal B, Saadi S, Koriche N, Bouguelia A, Trari M (2009) Physical properties of the delafossite  $\text{LaCuO}_2$ . *J Phys Chem Solids* 70:1132–1136
- Gotzendorfer S (2011) Synthesis of copper-based transparent conductive oxides with delafossite structure via sol–gel processing. Ph. D Thesis Wurzburg
- Kawazoe H, Yasukawa M, Hyodo H, Kurita M, Yanagi H, Hosono H (1997) P-type electrical conduction in transparent thin films of  $\text{CuAlO}_2$ . *Nature* 389:939–942
- Younsi M, Aider A, Bouguelia A, Trari M (2005) Visible light-induced hydrogen over  $\text{CuFeO}_2$  via  $\text{S}_2\text{O}_3^{2-}$  oxidation. *Sol Energy* 78:574–580
- Brahimi R, Bessekhoud Y, Nasrallah N, Trari M (2012) Visible light  $\text{CrO}_4^{2-}$  reduction using the new  $\text{CuAlO}_2/\text{CdS}$  hetero-system. *J Hazard Mater* 219–220:19–25
- Omeiri S, Gabes Y, Bouguelia A, Trari M (2008) Photoelectrochemical characterization of the delafossite  $\text{CuFeO}_2$ : application to removal of divalent metals ions. *J Electroanal Chem* 614:31–40
- Kato S, Fujimaki R, Ogasawara M, Wakabayashi T, Nakahara Y, Nakata S (2009) *Appl Catal B* 89:183–188
- Brahimi R, Rekhila G, Bessekhoud Y, Trari M (2014) Crystal growth and transport properties of  $\text{CuAlO}_2$  single crystal. *Crystallogr Rep* 59(7):1088–1092
- Derbal A, Omeiri S, Bouguelia A, Trari M (2008) Characterization of new heterosystem  $\text{CuFeO}_2/\text{SnO}_2$  application to visible-light induced hydrogen evolution. *Int J Hydrogen Energy* 33:4274–4282
- Omeiri S, Allalou N, Rekhila G, Bessekhoud Y, Trari M (2013) Preparation and characterization of nano structured  $\text{Ba}_2\text{SnO}_4$  as a novel photocatalyst material for the chromate reduction. *Appl Nanosci*. doi:10.1007/s13204-013-0276-z
- Sakka S (2005) In: Kozuka H (ed) *Handbook of sol gel science and technology*. Processing characterization and applications. vol 1, chap 2, pp 129–170. Kluwer Academic Publishers, Boston
- Koseva I, Chaminade JP, Gravereau P, Pechev S, Peshev P, Etourneau JA (2005) New family of isostructural titanates,  $\text{MLi}_2\text{Ti}_6\text{O}_{14}$  (M = Sr, Ba, Pb). *J Alloys Compds* 389(1–2):47–54
- Aegerter MA, Menning M (2004) *Sol-gel technologies for glass producers and users*. Kluwer Academic Publisher, Germany
- Kezzim A, Nasrallah N, Abdi A, Trari M (2011) Visible light induced hydrogen on the novel heterosystem  $\text{CuFe}_2\text{O}_4/\text{TiO}_2$ . *Energy Convers Manag* 52(8):2800–2807
- Bassaid S, Chaib M, Omeiri S, Bouguelia A, Trari M (2009) Photocatalytic reduction of cadmium over  $\text{CuFeO}_2$  synthesized by sol–gel. *J Photochem Photobiol A20*:62–68
- Brostow W, Datashvili T (2008) Chemical modification and characterization of boehmite nanoparticles. *Chem Chem Technol* 2:27–32
- Jacob KT, Alcock CB (1975) Thermodynamics of  $\text{CuAlO}_2$  and  $\text{CuAl}_2\text{O}_4$  and phase equilibria in the system  $\text{Cu}_2\text{O}-\text{CuO}-\text{Al}_2\text{O}_3$ . *J Am Ceram Soc* 58:192–195
- Gadalla AMM, White J (1964) Equilibrium relationships in the system  $\text{CuO}-\text{Cu}_2\text{O}-\text{Al}_2\text{O}_3$ . *J Br Ceram Soc* 63:39–62
- Ingram BJ, Mason TO, Asahi R, Park KT, Freeman AJ (2001) Electronic structure and small polaron hole transport of copper aluminates. *Phys Rev B* 64:155114–155117
- Chen HY, Tsai MW (2011) Delafossite- $\text{CuAlO}_2$  films prepared by annealing of amorphous Cu–Al–O films at high temperature under controlled atmosphere. *Thin Solid Films* 519:5966–5970
- JCPDS Diffraction File, Card No. 075-2356
- Shannon RD (1976) Revised effective ionic radii and systematic studies of interatomic distances in halides and chalcogenides. *Acta Crystallogr A* 32:751–767
- Doumerc JP, Ammar A, Wichainchai A, Pochard M, Hagenmuller P (1987) Sur quelques nouveaux composés de structure de type delafossite. *J Phys Chem Solids* 48:37–40
- Saha B, Thapa R, Chattopadhyay KK (2009) A novel route for the low temperature synthesis of p-type transparent semiconducting  $\text{CuAlO}_2$ . *Mater Lett* 63:394–396
- Banarjee AN, Kundoo S, Chattopadhyay KK (2003) Synthesis and characterization of p-type transparent conducting thin film by DC sputtering. *Thin Solid Films* 440:5–10
- Ghosh CK, Popuri SR, Mahesh T, Chattopadhyay KK (2009) Preparation of nanocrystalline  $\text{CuAlO}_2$  through sol–gel route. *J Sol Gel Sci Technol* 52:75–81
- Khassin AA, Kustova GN, Jobic H, Yurieva TM, Chesalov AY, Filonenko AG, Plyasova LM, Parmon VN (2009) The state of absorbed hydrogen in the structure of reduced copper chromite from the vibration spectra. *Phys Chem Chem Phys* 11:6090–6097
- Pellicer PJ, Martínez-GD Segura A, Rodríguez-Hernández P, Muñoz A, Chervin JC, Garro N, Kim D (2006) Pressure and temperature dependence of the lattice dynamics of  $\text{CuAlO}_2$  investigated by Raman scattering experiments and ab initio calculations. *Phys Rev B* 74:184301–184308
- Lan W, Cao WL, Zhang M, Liu XQ, Wang YY, Xie EQ, Yan H (2009) Annealing effect on the structural, optical and electrical properties of  $\text{CuAlO}_2$  films deposited by magnetron sputtering. *J Mater Sci* 44:1594–1599
- Elkhouni T, Amami M, Strobel P, Ben Salah A (2013) Structural and magnetic properties of substitutes delafossite-type oxides  $\text{CuCr}_{1-x}\text{Sc}_x\text{O}_2$ . *World J of Condens Matter Phys* 3:1–8
- Nagabhushana KR, Lakshminarasappa BN, Singh F (2009) Photo luminescence and Raman studies in swift heavy ion irradiated polycrystalline aluminum oxide. *Bull Mater Sci* 32:515–519
- Kadleřková M, Breza J, Veselý M (2001) Raman spectra of synthetic sapphire. *Microelectronics J* 32:955–958
- Lübbe M, Gigler AM, Stark RW, Moritz W (2010) Identification of iron oxide phases in thin films grown on  $\text{Al}_2\text{O}_3$  (0 0 1) by Raman spectroscopy and X-ray diffraction. *Surf Sci* 604:679–685
- Pankov JI (1971) *Optical Processes in Semiconductors*. Prentice-Hall Inc., Englewood Cliffs, p 31
- Banarjee AN, Chattopadhyay KK (2008) P Type transparent semiconducting delafossite  $\text{CuAlO}_{2+x}$  thin film: promising

- 
- material for optoelectronic devices and field emission displays. In: Olivante LV (ed) *Materials science research trends*, chap 1, pp 17–132. Nova Science Publishers, New York
38. Benko FA, Koffyberg FP (1984) Opto-electronic properties of  $\text{CuAlO}_2$ . *J Phys Chem Solids* 45(1):57–59
  39. Singh M, Rao AR, Dutta V (2008) Effect of pH on structural and morphological properties of spray deposited p-type transparent conducting oxide  $\text{CuAlO}_2$  thin films. *Mater Lett* 62(21–22): 3613–3616
  40. Tate J, Ju HL, Moon JC, Zakutayev A, Richard AP, Russel J, McIntyre DH (2009) Origin of p-type conduction in single-crystal  $\text{CuAlO}_2$ . *Phys Rev B* 80:165206 (1–8)
  41. Ingram BJ, Harder BJ, Hrabe NW, Mason TO (2004) Transport and defect mechanisms in cuprous delafossites  $\text{CuScO}_2$  and  $\text{CuYO}_2$ . *Chem Mater* 16(26):5623–5629
  42. Thomas J (1997) Materials science: invisible circuits. *Nature* 389:907–908
  43. Zhao S, Li M, Liu X, Han G (2009) Synthesis of  $\text{CuAlO}_2$  nanofibrous mats by electrospinning. *Mater Chem Phys* 116: 615–618
  44. Jun L, Xiang L, Hui Z, Yunbiao D, Qingmei C, Minggang C, Shaochun Z (2011) Preparation and performance of  $\text{CuAlO}_2$  ceramic target. *Powder Metall Technol* 29(3):12–15
  45. Töpfer J, Trari M, Doumerc JP (2007) Preparation and physical properties of  $\text{CuAl}_{1-x}\text{Mn}_x\text{O}_2$  ( $0 \leq x \leq 0.2$ ) delafossites. *Solid State Sci* 9:236–239
  46. Benreguia N, Omeiri S, Bellal B, Trari M (2011) Visible light induced  $\text{H}_2\text{PO}_4^-$  removal over  $\text{CuAlO}_2$  catalyst. *J Hazard Mater* 192:1395–1400
  47. Ruttanapuna C, Kosalwata W, Rudradawong C, Jindajitawat P, Buranasiria P, Naenkieng D, Boonyopakorn N, Harnwungmoung A, Thowladda W, Neeyakorn W, Thanachayanont C, Charoenphakdee A, Wichainchai A (2014) Reinvestigation thermoelectric properties of  $\text{CuAlO}_2$ . *Energy Procedia* 56:65–71
  48. Brahimi R, Bellal B, Bessekhoud Y, Bouguelia A, Trari M (2008) Physical properties of  $\text{CuAlO}_2$  single crystal. *J Cryst Growth* 310:4325–4329